Research Article GU J Sci, Part A, 13(2): 906-924 (2026) 10.54287/gujsa.1951854

Gazi University
Journal of Science
PART A: ENGINEERING AND INNOVATION
http://dergipark.org.tr/gujsa

Investigation of Induced Radioactivity and Dose Distribution in Proton-Irradiated Nitinol SMA at 8.5, 25.5 and 42.5 MeV using FLUKA Simulation

Berkay ÇAKIR[1*] Uğur GÖKMEN[1]

[1] Gazi University, Institute of Science and Technology, Department of Metallurgical and Materials Engineering, Ankara, Türkiye

Keywords

Nitinol
Proton Irradiation
Residual Dose
Induced Activity
FLUKA
FLAIR

Abstract

In this study, the dose distribution and induced radioactivity of a proton-irradiated Nitinol (NiTi) shape memory alloy plate with dimensions of 2 × 1 × 0.3 cm were investigated using the FLUKA Monte Carlo code at three different proton energy values of 8.5, 25.5, and 42.5 MeV under a constant beam intensity of 2.0×10^{13} p/s. Simulations carried out through the FLUKA/FLAIR interface were used to evaluate the total specific activity, activation-product inventory, residual ambient dose equivalent H*(10) distributions, and neutron fluence spectra at the end of irradiation and after cooling times of 1 hour, 1 day, and 1 week. The results showed that ^{47}V was the dominant radionuclide in all energy scenarios. The total specific activity of the sample after irradiation increased from around 1.00×10^{7} Bq/g for 8.5 MeV to about 1.12×10^{9} Bq/g for 25.5 MeV and 2.30×10^{9} Bq/g for 42.5 MeV, respectively, corresponding to an approximately 230-fold increase across the considered energy range. The co-production of ^{48}V and ^{64}Cu for the 8.5 MeV case is consistent with the radionuclide inventory reported in brachytherapy-oriented activation studies of Nitinol. Maps for residual dose distribution showed that there was maximum radiation field intensity at the center of the implant, which quickly decayed in the initial phase of cooling; however, it remained at high levels after longer cooling time in the higher energy cases. The neutron fluence spectra likewise showed a systematic increase in the secondary radiation field with increasing proton energy, in agreement with the observed activation inventory. Overall, the results provide a structured picture of the energy-dependent activation and dose behavior of proton-irradiated Nitinol. These findings provide a reliable basis for radiation safety assessment, cooling-time optimization, and the planning of future implant-focused proton dosimetry studies.

Cite

Çakır, B., & Gökmen, U. (2026). Investigation of Induced Radioactivity and Dose Distribution in Proton-Irradiated Nitinol SMA at 8.5, 25.5 and 42.5 MeV using FLUKA Simulation. *GU J Sci, Part A*, *13*(2), 906-924. doi:10.54287/gujsa.1951854

Author ID (ORCID Number)

0009-0001-5500-9438 Berkay ÇAKIR
0000-0002-6903-0297 Uğur GÖKMENE

Article Process

Submission Date 15.05.2026
Revision Date 24.05.2026
Accepted Date 30.06.2026
Published Date 30.06.2026

1. INTRODUCTION

Nitinol (NiTi), a near-equiatomic nickel-titanium shape memory alloy (SMA), has emerged as a promising smart material in the design of medical devices due to its unique combination of superelasticity, shape memory effect, biocompatibility, and relatively strong corrosion resistance (Morgan, 2004; Aboutalebi et al., 2015). The ability of the alloy to undergo reversible martensitic phase transformations greatly enables its applications, ranging from cardiovascular stents and guidewires to orthodontic archwires and surgical instruments (Duerig et al., 1999). More recently, the convergence of advances in Nitinol materials with radiation medicine has opened new research areas, especially in the development of radioactive stents for intravascular brachytherapy and the radiological behavior of metallic implants in high-radiation environments (Eigler et al., 1999; Arbabi

*Corresponding Author, e-mail: berkaycakir@gazi.edu.tr

This work is licensed under Creative Commons Attribution-ShareAlike 4.0 International.

et al., 2009). Beyond brachytherapy, NiTi alloys are increasingly encountered in space systems, nuclear engineering, and biomedical environments where radiation exposure is unavoidable. Accordingly, radiation interactions in different SMAs have been extensively investigated through both simulations and in situ experiments. The results indicate irradiation-induced changes in mechanical and physical properties as well as microstructure after radiation exposure (Dughaish, 1997; Tatar & Zengin, 2005; Saud et al., 2014). As a proton beam passes through a metallic target, it loses energy mainly via ionization, multiple Coulomb scattering, and hadronic interactions. This deposits energy locally and, at the same time, drives several secondary effects: the production of secondary particles, displacement damage in the lattice, and the activation of target nuclei, the latter of which can give rise to short- and medium-lived radionuclides (Agosteo et al., 1998; Stoller et al., 2013; Siddiqui et al., 2023; Yu & Chen, 2024). Understanding the spatial distribution of energy deposition, absorbed dose, and induced radioactivity is therefore essential for optimizing performance of the related applications, ensuring radiation safety, and predicting long-term material behavior (Schneider et al., 2002).

Producing vanadium-48 (V-48) by proton activation of the titanium isotopes present in Nitinol has drawn considerable interest as a route to brachytherapy sources (Li et al., 1998; Eigler et al., 1999; Arbabi et al., 2009; Sadeghi et al., 2011). A mixed beta–gamma emitter with a 15.97-day half-life and a β^+ branching ratio of 49.5%, V-48 can deliver therapeutic doses directly to vessel walls, which has made it an potential candidate for intravascular brachytherapy (Nath et al., 1999; Sadeghi et al., 2011; Chen, 2022). The 5–15 MeV proton energy window is important because the main nuclear reaction channel, ^{48}Ti(p,n)^{48}V, occurs within this interval, making this energy range particularly crucial for medical isotope production (Sadeghi et al., 2012). Proton activation of nickel and trace elements also produces other radionuclides such as copper-64 (Cu-64), cobalt isotopes, and various zinc isotopes, each contributing to the overall activity inventory and dose distribution (Anwer et al., 2022; Muhammad et al., 2025).

Monte Carlo simulation has become the standard approach for predicting radiation transport, energy deposition, and activation across a wide range of geometries (Böhlen et al., 2014). The FLUKA Monte Carlo code is a complete and integrated tool for simulating all aspects of particle physics problems, from thermal neutrons up to high energy particles of cosmic rays. It combines detailed physics models for electromagnetic interactions, hadronic cascades, and low-energy neutron transport, a combination that makes it particularly well suited to activation and dosimetry studies (Ferrari et al., 2005; Böhlen et al., 2014; Battistoni et al., 2015). The code has been tested extensively on experimental data for proton interactions in various materials and is widely used in medical physics, radiation protection, and accelerator applications (Amin et al., 2018; More et al., 2023; Rafiei et al., 2025). Furthermore, several experimental studies have investigated proton-induced activation in Nitinol for medical applications, providing valuable benchmarks for validating the simulation results (Li et al., 1998; Arbabi et al., 2009; Sadeghi et al., 2011).

Li et al. (1998) developed a ^{48}V-emitting Nitinol stent for intracoronary brachytherapy by activating commercial stents with 8.5 ± 1.5 MeV protons in a cyclotron. The study showed that a ^{48}V-emitting Nitinol

stent, produced by proton activation of titanium atoms within the Nitinol alloy, could act as a localized mixed beta/gamma intravascular brachytherapy source for restenosis-related applications. Under their irradiation conditions, the authors reported an activity production rate of approximately 6.0 mCi per stent per hour, depending on irradiation conditions and stent geometry. In the present FLUKA calculation, the activity density was calculated as 6.45×10^7 Bq/cm³ for a 0.6 cm³ NiTi target volume, corresponding to a total activity of 3.87×10^7 Bq, or approximately 1.05 mCi. Since this value is averaged over a larger bulk NiTi target volume, it should not be directly compared with the activity density of a thin coronary stent. When this total activity is hypothetically normalized to the modeled stent metal volume reported by Li et al. (1998), approximately 3.7 mm³ or 0.0037 cm³, this corresponds to a stent-volume-normalized activity density of approximately 1.05×10^{10} Bq/cm³. Considering the real strut cross-section of approximately 180 × 240 μm, the corresponding value would be approximately 6.2×10^9 Bq/cm³. Therefore, the normalized activity density is approximately in the order of 10^9–10^{10} Bq/cm³, in reasonable agreement with the activity level expected for activated thin Nitinol stent geometries. This comparison should be interpreted as a geometry-based normalization rather than a direct one-to-one validation.

Arbabi et al. (2009) subsequently characterized the dosimetry of proton-activated Nitinol stents for renal artery brachytherapy by irradiating them with 8.5 MeV protons and measuring an average contact dose rate of 37 mGy/h after 3 days of cooling at an initial activity of approximately 6 μCi (~0.22 MBq). Normalizing this measurement to unit activity yields approximately 168 mGy/h per MBq. In the present FLUKA simulation at 8.5 MeV, the total activity of the bulk NiTi target was found to be approximately 38.7 MBq (1.00×10^7 Bq/g × 3.87 g) at end of irradiation (EOI), and it decreased to about 2.55 MBq after 3 days of cooling, mainly due to the residual contribution of ^{48}V and ^{64}Cu. When the corresponding simulated contact-surface H*(10) rate at 3 days was normalized to unit activity, a value of approximately 195 ± 18 mGy/h per MBq was obtained, which is in good agreement with the experimental value of 168 mGy/h per MBq reported by Arbabi et al. (2009). The relative deviation between the two values is about 16 %, and it is consistent with the experimental uncertainty of around 10 % reported in (Arbabi et al., 2009), as well as with the geometric simplification adopted in the present simulation, in which a flat plate geometry was used instead of a cylindrical stent. This level of agreement provides further support for the overall consistency of the activation and dose calculations obtained in the 8.5 MeV regime, where the dominant ^{48}Ti(p,n)^{48}V reaction channel is known to have well-characterized cross sections.

Despite extensive work on proton-activated Nitinol stents (Li et al., 1998; Eigler et al., 1999; Arbabi et al., 2009; Sadeghi et al., 2011), experimental and computational studies characterizing the effect of proton irradiation distribution of energy deposition, dose, and activation products are relatively scarce. Previous research has largely focused on either the production yields for specific isotopes (Sadeghi et al., 2012; Amin et al., 2018; Anwer et al., 2022; Muhammad et al., 2025), or the microstructural effects of proton irradiation on phase transformations (Dughaish, 1997; Z. G. Wang et al., 2003; H. Wang et al., 2018; Yi et al., 2022).

However, comprehensive energy-resolved evaluations that simultaneously address total specific activity, residual ambient dose equivalent, secondary neutron fluence spectra, and the complete activation-product inventory remain scarce.

In this work, we use FLUKA to systematically simulate a Nitinol plate irradiated at 8.5, 25.5, and 42.5 MeV under a constant proton flux of 2.0×10^{13} p/s. The study aims to quantify the total specific activity and identify the dominant activation products at each energy, to map the spatial distribution of H*(10) at multiple cooling times, to analyze the neutron fluence spectra and their energy dependence, and to provide a structured dataset that supports radiation safety assessment, cooling-time planning, and future implant-focused dosimetry studies. The results provide a quantitative basis for evaluating activation yields in proton-irradiated Nitinol, for radiation-protection assessments related to such activated components, and for understanding radiation-induced material modifications.

The simulation utilizes FLAIR (FLUKA Advanced Interface) for geometry construction and visualization and employs multiple scoring techniques to systematically characterize the radiation field and activation products.

2. MATERIAL AND METHOD

2.1. Simulation Design

Systematic Monte Carlo simulations were carried out with the FLUKA code through the FLAIR graphical interface. The FLUKA model is chosen because it considers both hadron and electromagnetic processes under the same transport model, employs multigroup cross-sections for low-energy neutrons, and performs residual activity calculations using the RADDECAY module (Ferrari et al., 2005; Böhlen et al., 2014; Battistoni et al., 2015). Moreover, the reliability of the FLUKA simulation for proton dosimetry and activation studies in this research is also confirmed by recent benchmarks and validation studies (Amin et al., 2018; Rafiei et al., 2025; Şerban et al., 2025).

All simulations were performed using FLUKA version 4-5.0 together with the FLAIR graphical interface (version 3.4-3). The target shape was modeled as a rectangular Nitinol shape memory alloy plate with dimensions of $2.0 \times 1.0 \times 0.3$ cm, corresponding to a volume of 0.60 cm^3. The alloy density was taken as 6.45 g/cm^3, resulting in a target mass of 3.87 g. The NiTi composition was defined as a near-equiatomic Ni–Ti binary mixture with mass fractions of 55.0% Ni and 45.0% Ti, corresponding to the nominal 50.6 at.% Ni stoichiometry of commercial Nitinol. The NiTi plate was selected as the target and placed inside the scoring volume, while the surrounding region was filled with air to estimate the target's intrinsic post-irradiation radiological properties. A quasi-monoenergetic proton beam (0.45 MeV FWHM energy spread), normally incident on the 2.0×1.0 cm plate surface, was applied under three irradiation scenarios at 8.5, 25.5, and 42.5 MeV. The beam was defined with a circular Gaussian profile (FWHM = 2.0 cm) centered on the plate, with negligible angular divergence; the source point was placed 5 cm upstream of the target surface in air. The beam width was deliberately chosen to be larger than the plate to ensure spatially uniform proton coverage across

the entire implant surface. In each case, the proton beam intensity was kept constant at 2.0×10^{13} p/s, corresponding to an approximate beam current of 3.2 μA. For all cases, the duration of irradiation was fixed at 1 h, resulting in a total proton fluence of 7.2×10^{16}. The above energies were chosen because they cover both the low energy activation window suitable for producing ^{48}V and high energies where other nuclear reactions take place (Sadeghi et al., 2012; Anwer et al., 2022; Muhammad et al., 2025). Table 1 summarizes the principal irradiation parameters.

Table 1. *Principal input parameters used in all irradiation scenarios.*

Parameter	8.5 MeV	25.5 MeV	42.5 MeV
Proton flux, I	2.0×10^{13} p/s	2.0×10^{13} p/s	2.0×10^{13} p/s
Beam current	~3.2 μA	~3.2 μA	~3.2 μA
Irradiation time	1 hour	1 hour	1 hour
Total fluence	7.2×10^{16} p	7.2×10^{16} p	7.2×10^{16} p
Residual dose cooling times	EOI, 1 h, 1 d, 1 w	EOI, 1 h, 1 d, 1 w	EOI, 1 h, 1 d, 1 w
Activation output	Isotopic and total specific activity	Isotopic and total specific activity	Isotopic and total specific activity
Fluence output	E·dΦ/dE	E·dΦ/dE	E·dΦ/dE

2.2. Physics Settings and Scoring

The physical settings in FLUKA were set up to make sure that hadronic cascades, radioactivity decays, and residual doses could be accurately treated within the energy range studied. The default physical settings of PRECISIO were employed as the initial physical settings, which activates the PEANUT (Pre-Equilibrium Approach to Nuclear Thermalization). PEANUT is generalized intranuclear cascade model for proton-induced reactions across the whole energy investigated in this work. In addition to the PRECISIO defaults, the coalescence of light fragments (PHYSICS, COALESCE) and the evaporation of heavy fragments (PHYSICS, EVAPORAT) were explicitly activated to improve the treatment of light-fragment and residual-nucleus production. Residual activity calculations and the time evolution of radioactive decay were enabled using the RADDECAY card, which relies on the internal FLUKA decay-data library. The simulations were carried out with the PRECISIO defaults. Since no additional EMFCUT card was used, the electron, positron and photon transport thresholds followed the default electromagnetic transport settings of FLUKA. Low-energy neutrons were transported down to thermal energies using the neutron transport treatment available in FLUKA. The irradiation profile was defined with the IRRPROFI card for an irradiation time of 1 h at constant intensity, and the post-irradiation cooling times EOI, 1 h, 1 d, 1 w were specified with the DCYTIMES card.

The main quantities were scored using the following FLUKA estimators. The RESNUCLEI card was used to obtain isotope-resolved and total specific activities in Bq/g at EOI and after cooling. Residual ambient dose

equivalent rate, H*(10), was scored using USRBIN together with the AMB74 fluence-to-dose conversion set on a Cartesian mesh of 30 × 30 × 30 cm³ centered on the target (−15 to +15 cm along each axis) with 100 × 100 × 100 bins, corresponding to a spatial resolution of 0.3 cm per bin, from which two-dimensional maps in the plane of the implant were extracted. The neutron fluence spectrum inside the NiTi volume was evaluated with USRTRACK using logarithmic energy binning and expressed in the lethargy representation, E·dΦ/dE. Each irradiation scenario was simulated with 5 independent statistical runs of 2 × 10^8 primary protons (1 × 10^9 histories in total), which kept the relative statistical uncertainty below 5 % for all major activation products reported in Table 2–4 and below 10 % for the H*(10) maps in the high-dose region around the implant. This combination of scorers made it possible to examine the activation inventory, the time-dependent activity decline, the residual external radiation field, and the energy dependence of the secondary neutron field within a single simulation workflow (Ferrari et al., 2005; Böhlen et al., 2014; Battistoni et al., 2015).

2.3. Physical Formalism

The production rate of radionuclide i may be written as

$$\mathrm{P_i(E)} = \Phi_\mathrm{p} \cdot \mathrm{N_T} \cdot \sigma_\mathrm{i}(\mathrm{E}) \tag{1}$$

where Φ_p is the proton flux (p/s), N_T is the number of target atoms per unit mass, and $\sigma_i(E)$ is the energy-dependent reaction cross section for channel i. After an irradiation time t_{irr} and a cooling time t_c, the specific activity of radionuclide i can be expressed as

$$A_i(t_c) = P_i(E) \cdot \left(1 - e^{-\lambda_i \cdot t_{irr}}\right) \cdot e^{-\lambda_i \cdot t_c} \tag{2}$$

where $\lambda_i = \ln(2)\,/T_{1/2,i}$ is the decay constant. The total specific activity is then obtained by summing over all produced radionuclides:

$$A_{total}(t_c) = \sum_i A_i(t_c) \tag{3}$$

The residual ambient dose equivalent rate at position r and cooling time t may be written as

$$H^*(10, r, t) = \sum_k \Phi_k(r, t) \cdot h_k \tag{4}$$

where $\Phi_k(r, t)$ is the fluence of radiation type k at position r and time t, and h_k is the corresponding fluence-to-ambient-dose-equivalent conversion coefficient (Pelliccioni, 2000; Ferrari et al., 2005). In the present work, these quantities were not evaluated analytically but extracted from the FLUKA USRBIN scorer described above; the equations are provided to define the physical meaning of the reported outputs.

3. RESULTS AND DISCUSSION

3.1. Activation Products and Specific Activity at the End of Irradiation

At EOI, the activation inventory was dominated by a limited number of radionuclides, although both the total activity level and the isotopic diversity increased strongly with proton energy. In all three scenarios, ^{47}V was identified as the dominant radionuclide, confirming that activation of the Ti component governs the early post-irradiation behavior of NiTi in the investigated energy range.

For the 8.5 MeV scenario, the total specific activity at EOI was approximately 1.00×10^7 Bq/g. The leading contributors were ^{47}V, ^{62}Cu, and ^{11}C, while the simultaneous presence of ^{48}V and ^{64}Cu remained one of the most important features of the low-energy case. The ^{48}V specific activity at EOI was 4.39×10^5 Bq/g (4.39 % of the total), corresponding to a total ^{48}V activity of approximately 1.70 MBq in the 3.87 g target; the ^{64}Cu contribution was 1.13×10^5 Bq/g (~0.44 MBq total). For reference, the proton-activated Nitinol stents reported by Arbabi et al. (2009) reached an initial activity of ~0.22 MBq before clinical handling, and earlier intravascular brachytherapy work (Li et al., 1998; Nath et al., 1999; Sadeghi et al., 2011) has indicated that ^{48}V end-of-irradiation activities of the order of 0.1–1 MBq per device are within the therapeutically useful range. Accordingly, the present 8.5 MeV simulation already produces a ^{48}V activity of approximately 1.70 MBq, which is about 7.7 times higher than the ~0.22 MBq reported by Arbabi et al. (2009) and lies slightly above the upper bound of the 0.1–1 MBq range reported in earlier intravascular brachytherapy studies (Li et al., 1998; Nath et al., 1999; Sadeghi et al., 2011). Shorter irradiation times or reduced beam currents could therefore be used to adjust the ^{48}V yield toward that reported range, depending on the intended device geometry and post-irradiation handling requirements. However, direct clinical applicability would still require dedicated experimental validation. The concurrent production of ^{64}Cu is also of interest for activation studies on NiTi alloys irradiated by low-energy proton beams.

At 25.5 MeV, the total specific activity increased sharply to about 1.12×10^9 Bq/g, corresponding to an approximately 112-fold increase relative to 8.5 MeV. Although ^{47}V remained the dominant radionuclide, the activation inventory became significantly richer. In addition to ^{47}V, the most important contributors were ^{60}Cu, ^{58}Cu, and ^{45m}Sc, indicating that several intermediate-threshold channels of nuclear reactions in Ni and Ti became effective in this energy region (Sadeghi et al., 2012; Anwer et al., 2022; Muhammad et al., 2025).

At 42.5 MeV, the total specific activity reached approximately 2.30×10^9 Bq/g, corresponding to an approximately 230-fold increase relative to the 8.5 MeV case and an approximately 2.05-fold increase relative to 25.5 MeV. The major activation products at this point include ^{47}V, ^{45m}Sc, and ^{58}Cu, as well as other short-lived and medium-lived radionuclides. Thus, an increase in the proton energy does not only increase the activity but also broadens the reaction channel range (Sadeghi et al., 2012; Anwer et al., 2022; Muhammad et al., 2025). It should be noted that the 19 radionuclides listed in Table 4 account for approximately 97.6 % of the total specific activity at this energy, compared with 99.99 % at 8.5 MeV and 99.67 % at 25.5 MeV; the remaining ~2.4 % at 42.5 MeV is distributed among a long tail of minor short-lived ($T_{1/2}$ < 1 min) and very-

low-yield channels, none of which individually exceeds 0.5 % of the total activity. This broader long tail is a direct consequence of the larger number of accessible spallation and pre-equilibrium channels opened at 42.5 MeV.

Table 2, 3, and 4 show the major activation products at EOI for the 8.5, 25.5, and 42.5 MeV scenarios, respectively. Table 5 provides a direct comparison of the three cases in terms of the total specific activity and the dominant radionuclides.

Table 2. *Principal activation products in the NiTi sample at 8.5 MeV (t = 0, EOI).*

Radionuclide	Half-life	Specific activity (Bq/g)	Fraction of total activity (%)
47V	32.6 min	3.788E+06	37.86
62Cu	9.672 min	3.660E+06	36.58
11C	20.334 min	1.354E+06	13.53
48V	15.9735 d	4.393E+05	4.39
60Cu	23.7 min	2.693E+05	2.69
61Cu	3.343 h	1.366E+05	1.37
64Cu	12.7004 h	1.128E+05	1.13
46m1Sc	18.75 s	5.685E+04	0.57
14O	70.696 s	4.134E+04	0.41
13N	9.965 min	3.562E+04	0.36
46m2Sc	9.4 μs	3.101E+04	0.31
44Sc	4.0421 h	2.571E+04	0.26
44m2Sc	154.8 ns	2.067E+04	0.21
45mSc	318 ms	1.550E+04	0.15
58m2Co	10.5 μs	1.034E+04	0.10
15O	122.24 s	5.168E+03	0.05
49V	330 d	2.070E+03	0.02
58m1Co	8.853 h	1.744E+03	0.02
44m1Sc	58.61 h	6.076E+02	0.01
Total activity ratio of 19 nuclides			99.9986 %

Table 3. *Principal activation products in the NiTi sample at 25.5 MeV (t = 0, EOI).*

Radionuclide	Half-life	Specific activity (Bq/g)	Fraction of total activity (%)
47V	32.6 min	3.150E+08	28.16
60Cu	23.7 min	2.362E+08	21.11
58Cu	3.204 s	1.865E+08	16.67
45mSc	318 ms	1.045E+08	9.34
62Cu	9.672 min	8.212E+07	7.34
46V	422.62 ms	5.912E+07	5.29
46mV	1.02 ms	2.956E+07	2.64
45Ti	184.8 min	2.791E+07	2.49
46mSc	9.4 μs	1.800E+07	1.61
61Cu	3.343 h	1.546E+07	1.38
59Cu	81.5 s	1.267E+07	1.13
57Ni	35.60 h	9.443E+06	0.84
44Sc	4.0421 h	7.036E+06	0.63
48V	15.9735 d	4.287E+06	0.38
43Sc	3.891 h	2.371E+06	0.21
55Co	17.53 h	1.911E+06	0.17
60mCo	10.467 min	1.014E+06	0.09
58mCo	8.853 h	1.013E+06	0.09
42mSc	61.7 s	7.855E+05	0.07
Total activity ratio of 19 nuclides			99.6675 %

Table 4. *Principal activation products in the NiTi sample at 42.5 MeV (t = 0, EOI).*

Radionuclide	Half-life	Specific activity (Bq/g)	Fraction of total activity (%)
47V	32.6 min	6.579E+08	28.55
45mSc	318 ms	2.800E+08	12.15
58Cu	3.204 s	2.790E+08	12.11
46mSc	9.4 μs	2.162E+08	9.38
60Cu	23.7 min	1.535E+08	6.66
45Ti	184.8 min	1.193E+08	5.18
46V	422.62 ms	1.074E+08	4.66
53Fe	8.51 min	6.664E+07	2.89
62Cu	9.672 min	5.531E+07	2.40
59Cu	81.5 s	5.467E+07	2.37
46mV	1.02 ms	5.369E+07	2.33
44Sc	4.0421 h	5.075E+07	2.20
53mFe	2.54 min	3.362E+07	1.46
57Ni	35.6 h	3.299E+07	1.43
61Cu	3.343 h	1.942E+07	0.84
54Co	193.27 ms	1.884E+07	0.82
54mCo	1.48 min	1.884E+07	0.82
58mCo	8.853 h	1.799E+07	0.78
43Sc	3.891 h	1.384E+07	0.60
Total activity ratio of 19 nuclides			97.6318 %

Table 5. *Comparison of total specific activity and dominant radionuclides at EOI.*

Energy	Total specific activity (Bq/g)	Relative to 8.5 MeV	Three leading radionuclides
8.5 MeV	1.00×10^{7}	1.0	^{47}V, ^{62}Cu, ^{11}C
25.5 MeV	1.12×10^{9}	~112	^{47}V, ^{60}Cu, ^{58}Cu
42.5 MeV	2.30×10^{9}	~230	^{47}V, ^{45m}Sc, ^{58}Cu

3.2. Time-Dependent Activity Evolution

Activity reduction curves for all three cases show a two-phased pattern where the activity falls from the EOI stage until one week after exposure. Phase 1 is marked by a relatively fast fall of activity lasting from several minutes to about an hour due to the radioactive decay of short-lived radioisotopes such as 62Cu, 47V, 60Cu, and 58Cu. This process occurs especially quickly in the 25.5 and 42.5 MeV cases because of the large presence of short-lived reaction products.

The activity decay rate becomes slower in long-term cooling time. During this late phase, the activity curve is dominated by radionuclides with a longer half-life, such as 64Cu, 57Ni, 48V, and 49V if available. The reason behind the sharp drop in activity within the first few seconds after irradiation, yet the presence of activity after a week, especially in high-energy instances, is due to this trend. The relative bar graph at 1 hour, 24 hours, 72 hours, and 168 hours confirms that the highest activity is maintained in the 42.5 MeV case, followed by 25.5 MeV and 8.5 MeV.

Activity decay curves for each irradiation condition are presented in Figure 1 through 3. The rapid initial drop in total activity due mainly to the activity of the short-lived 47V, 62Cu, and 11C nuclides is succeeded by a gradual decrease after 1 hour, with remaining activities after 7 days due to 48V and 64Cu (Figure 1) at 8.5 MeV energy. At 25.5 MeV, where there is a much greater number of produced radionuclides, including 60Cu, 58Cu, and 45mSc, the slope of the decay curve is higher during the first stage and results in a higher level of activities maintained throughout the following period in comparison with those at 8.5 MeV (Figure 2). At 42.5 MeV, very short-lived elements, including 45mSc with its half-life of only 318 ms, contribute to the extremely fast activity decay, while the maintenance of activities throughout subsequent periods depends on 57Ni, 48V, and the whole scandium chain of nuclides (Figure 3). The bar chart presented in Figure 4 clearly shows that the activity difference between two investigated energies of about two orders of magnitude at 1 hour remains significant at each of the four cooling times used.

3.3. Residual Ambient Dose Equivalent Rate Distributions

Across all three energies, the residual H*(10) maps placed the strongest external radiation field located around the irradiated implant region. In all cases, the highest values appeared near the implant center, and the dose field decreased progressively away from the source region. This spatial pattern is consistent with the corresponding activation inventory, since radionuclide production was concentrated in the directly irradiated NiTi volume.

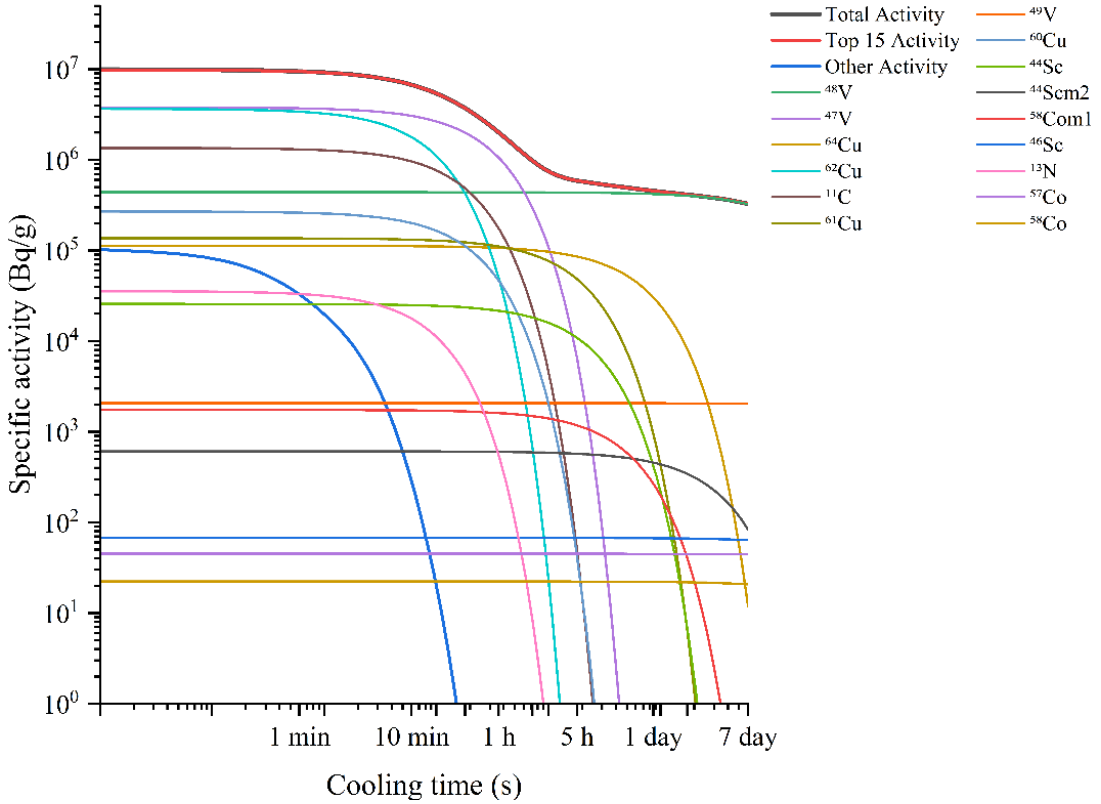


Figure 1. *Specific activity decay curves for the 8.5 MeV proton irradiation scenario. The top 15 contributing radionuclides and the total specific activity are shown as a function of cooling time from end of irradiation (EOI) to 7 days.*

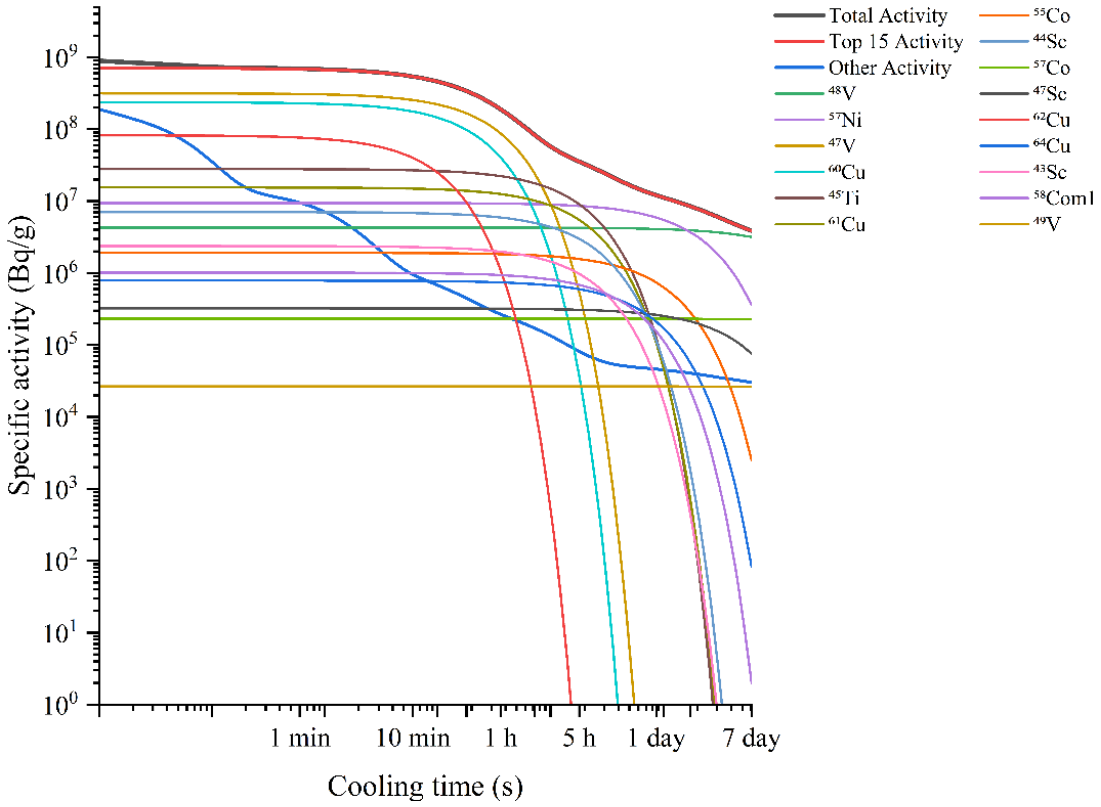


Figure 2. *Specific activity decay curves for the 25.5 MeV proton irradiation scenario. The top 15 contributing radionuclides and the total specific activity are plotted from EOI to 7 days.*

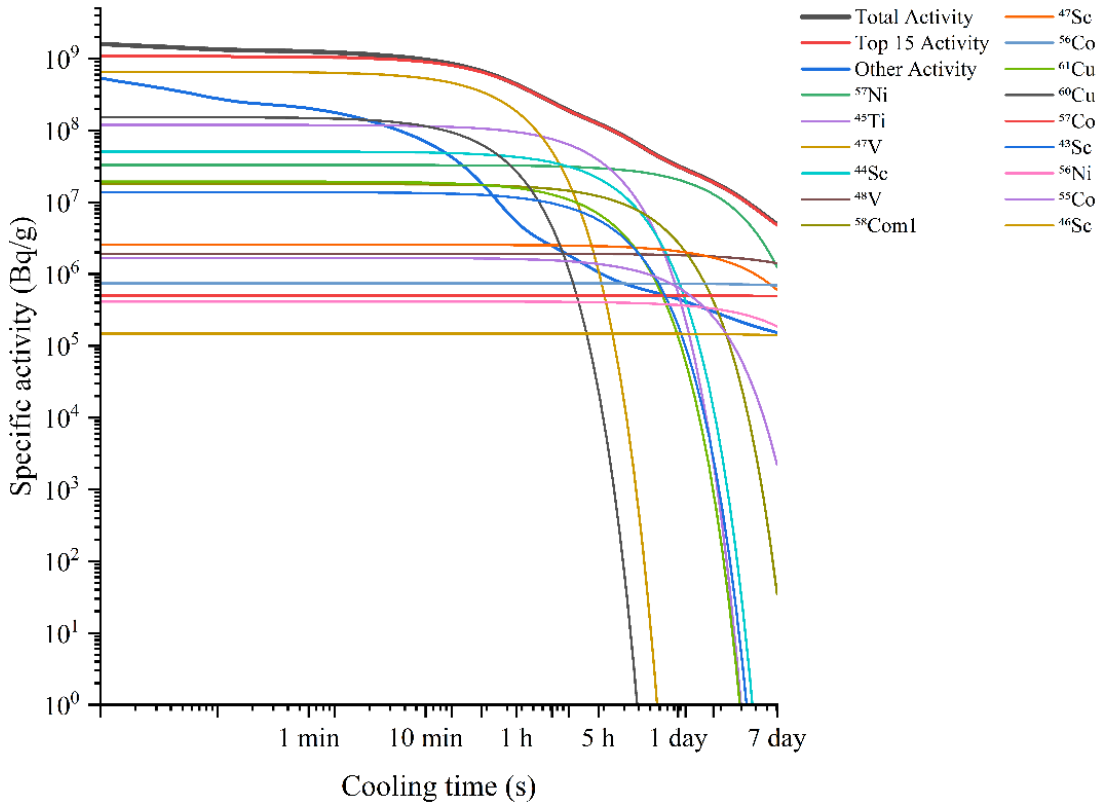


Figure 3. *Specific activity decay curves for the 42.5 MeV proton irradiation scenario. The top 15 contributing radionuclides and the total specific activity are shown from EOI to 7 days.*

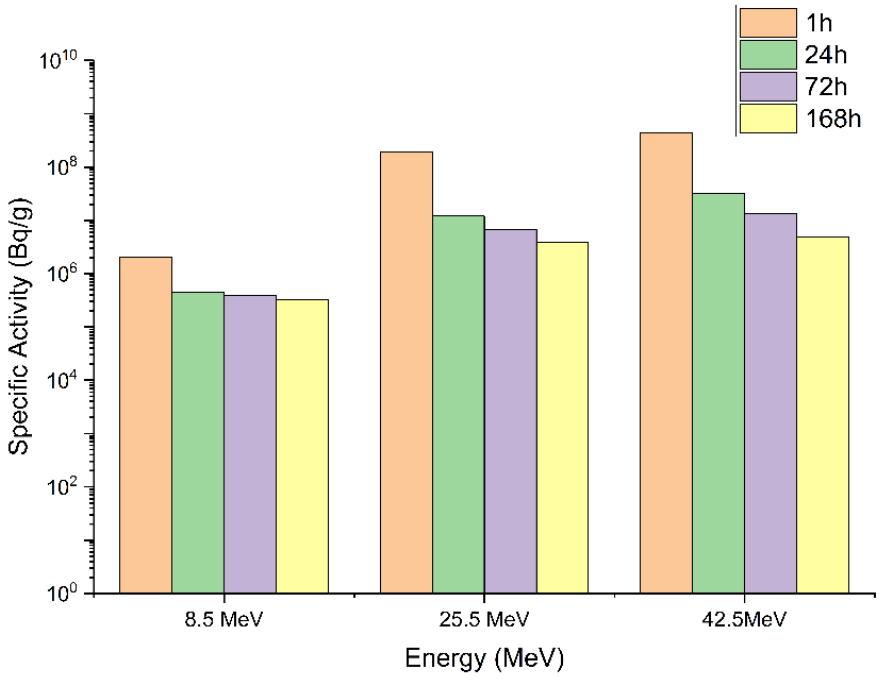


Figure 4. *Comparative bar chart of total specific activity at four cooling times (1 h, 24 h, 72 h, and 168 h) for the 8.5, 25.5, and 42.5 MeV irradiation scenarios.*

The 8.5 MeV case (Figure 5A) gave a residual field that was tightly confined to the immediate vicinity of the NiTi target at end-of-irradiation, with the peak H*(10) values sitting at the implant center and a steep radial fall-off beyond it. The field declined rapidly during the early cooling period: the 1 h and 1 d maps already

showed a marked decrease relative to EOI, and after 1 week the residual field had weakened substantially, although it remained measurable close to the implant.

The 25.5 MeV case (Figure 5B) showed the same general spatial pattern, but with markedly higher dose rates and a broader high-dose region. The richer inventory of Cu-, V-, and Sc-based activation products produced a stronger early external field and left a more visible residual component at 1 d and 1 week, so the field persisted longer during cooling than in the 8.5 MeV case.

The 42.5 MeV case (Figure 5C) produced the most intense and most spatially extended residual field of the three energies, and also the highest central H*(10) values. The high-dose region grew progressively with proton energy, reflecting both the larger number of accessible reaction channels and the contribution of secondary neutrons to the activation pattern. At a fixed beam current of 3.2 µA, this means that the external radiation field around an irradiated NiTi component scales strongly — and non-linearly — with the incident proton energy. Although the field dropped substantially over the first hour and the first day, a measurable signal persisted out to one week. The cooling-time evolution of the residual field is illustrated in detail for the 8.5 MeV case in Figure 6: after 1 h (Figure 6A) the distribution is still dominated by short-lived radionuclides such as ^{62}Cu, ^{47}V, and ^{58}Cu, producing a clearly defined high-dose region around the implant; by 1 d (Figure 6B) both the peak intensity and the spatial extent are substantially reduced, reflecting the decay of these short-lived contributors; and after 7 d (Figure 6C) the field is largely confined to the immediate neighborhood of the target, with the remaining signal mainly attributable to longer-lived radionuclides such as ^{48}V and ^{64}Cu. The sharp attenuation between the 1 h and 7 d maps shows that even at the lowest energy investigated here, an adequate cooling period is essential. The persistence seen at 42.5 MeV, on the other hand, reflects the contribution of longer-lived radionuclides and suggests that NiTi components irradiated at this higher energy would call for longer cooling times and stricter post-irradiation handling. Similar multi-stage residual-dose behavior has been seen in other proton-irradiation and accelerator-radiation studies, where the early-time field is set by short-lived products and the longer-term field by a smaller number of longer-lived radionuclides (Blaha et al., 2014; Yu & Chen, 2024).

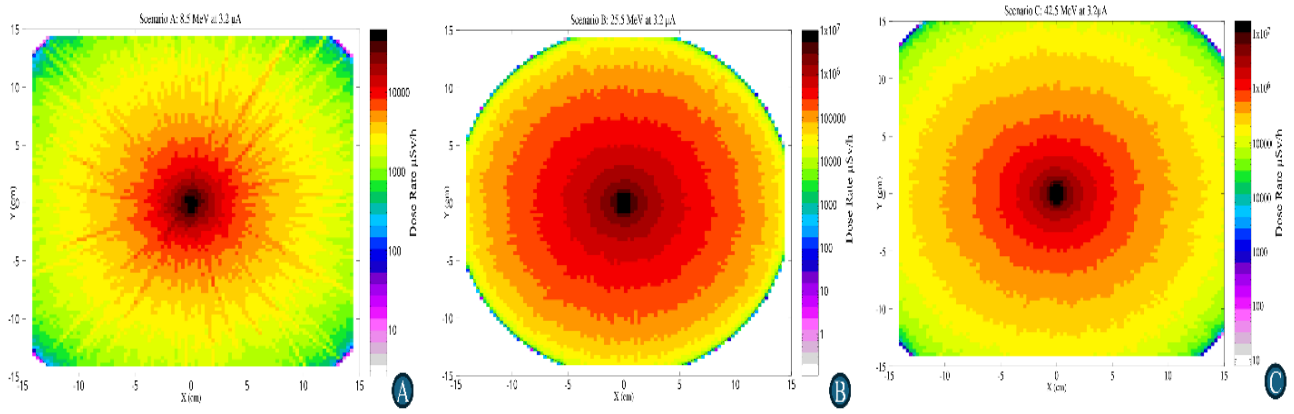


Figure 5. Residual ambient dose two-dimensional distribution at the downtime for three energy scenarios. Scenario A: 8.5 MeV (A), Scenario B: 25.5 MeV (B), Scenario C: 42.5 MeV (C) at 3.2 µA.

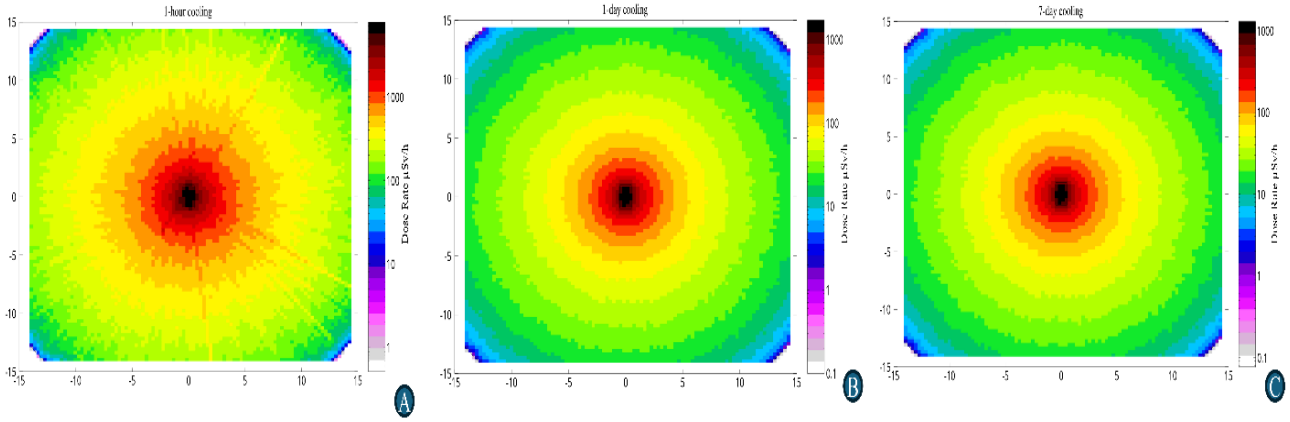


Figure 6. Residual ambient dose two-dimensional distribution at different cooling times for scenario A: (A) 1 hour cooling, (B) 1 day cooling, (C) 7 days cooling.

3.4. Neutron Fluence Spectra

The neutron fluence spectra inside the NiTi target exhibited a clear energy-dependent hierarchy. Across considered energy range, the highest neutron fluence was obtained for the 42.5 MeV case, which is followed by 25.5 MeV and 8.5 MeV. It becomes clearly visible in the intermediate and high-energy parts of the neutron spectrum that a rise in the proton energy not only boosts the number of produced neutrons but also expands the area of their distribution (Figure 7).

The observed relationship is consistent with the physical nature of activation. As proton energy increases, additional reaction channels become accessible, leading to enhanced secondary neutron production and a larger inventory of activation products. Thus, the neutron spectra support the interpretation derived from the activity data, indicating that higher proton energies result in stronger activation and higher residual dose levels.

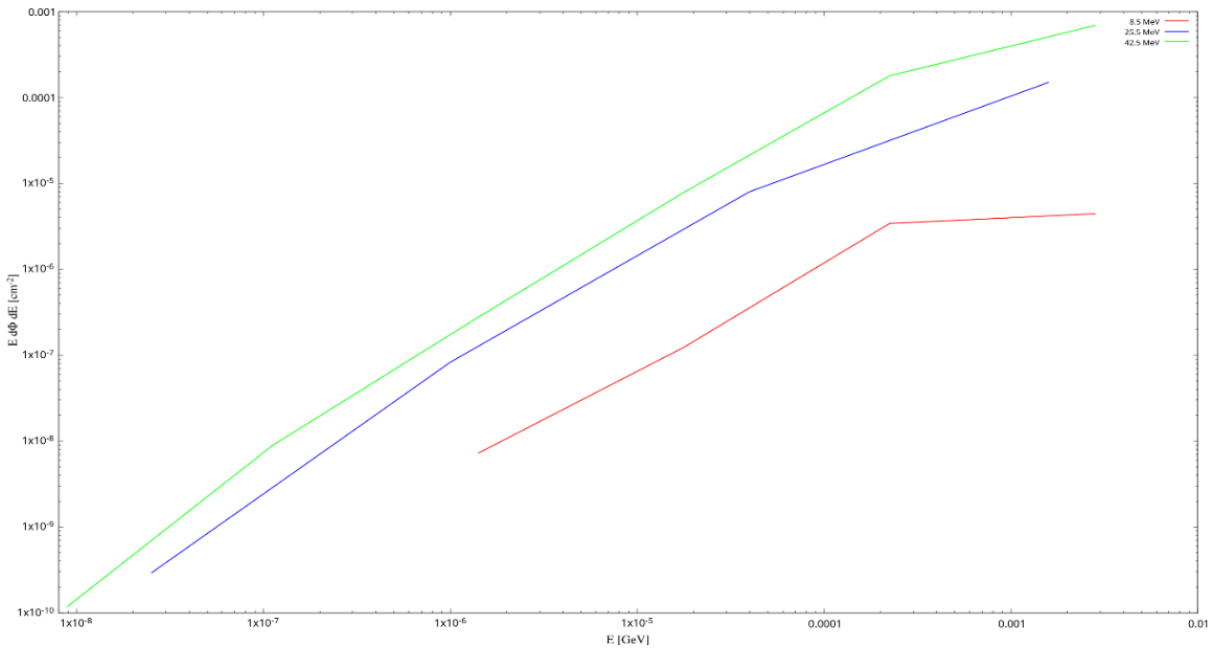


Figure 7. *Neutron fluence spectra E·dΦ/dE inside the NiTi target as a function of neutron energy (lethargy representation) for the 8.5, 25.5, and 42.5 MeV proton irradiation scenarios.*

4. CONCLUSION

The simulation study, using the FLUKA code, has provided a systematic study of the radiological properties of a Nitinol plate after irradiation with 8.5, 25.5, and 42.5 MeV protons at a constant beam intensity of 2.0×10^{13} p/s. In brief, the main findings are summarized as follows.

^{47}V was identified as the predominant activation product under the irradiation conditions considered in this study, contributing about 28–38 % of the total specific activity at EOI. The total specific activity showed a strong dependence on proton energy, increasing approximately 230-fold across the studied energy range, from 1.00×10^{7} Bq/g at 8.5 MeV to 1.12×10^{9} Bq/g at 25.5 MeV and 2.30×10^{9} Bq/g at 42.5 MeV.

Irradiation with 8.5 MeV protons leads to the simultaneous formation of ^{48}V and ^{64}Cu isotopes, indicating that the present results are relevant to brachytherapy-oriented activation studies and to medical-isotope production research; direct clinical use would require dedicated experimental validation. The obtained ambient dose equivalent maps corresponded well to the data on activated isotopes, as for each proton energy there were peak values near the implant center that decayed quickly in the early cooling time and stayed visible later during higher-energy irradiation scenarios. Similarly, the secondary neutron fluence spectra demonstrated an increasing trend in secondary neutron production with the increase of proton energy, providing a clear physical basis for the increased activation complexity and residual dose.

Overall, this study provides a comprehensive and energy-optimized activation and dose database for NiTi implants irradiated with proton beams. The resulting dataset offers a practical basis for radiation safety assessment, cooling-time optimization, and future implant-focused proton dosimetry studies.

AUTHOR CONTRIBUTIONS

Berkay Çakır: Investigation, Formal analysis, Writing – original draft, Methodology. Uğur Gökmen: Supervision, Methodology, Formal analysis.

AI Exclusion: AI tools are strictly prohibited from being listed as authors.

Legal Consent: All human authors confirm they have reviewed and legally accepted the final version under the **CC BY-SA 4.0** framework.

ACKNOWLEDGEMENT

I would like to express my sincere gratitude to Prof. Dr. Sema Bilge Ocak for her invaluable guidance, insightful feedback, and continuous support throughout this study.

CONFLICT OF INTEREST

The authors declare no conflict of interest.

REFERENCES

Aboutalebi, M. R., Karimzadeh, M., Salehi, M. T., Abbasi, S. M., & Morakabati, M. (2015). Influences of aging and thermomechanical treatments on the martensitic transformation and superelasticity of highly Ni-rich Ti-51.5at.% Ni shape memory alloy. *Thermochimica Acta*, *616*, 14–19. https://doi.org/10.1016/j.tca.2015.08.004

Agosteo, S., Birattari, C., Caravaggio, M., Silari, M., & Tosi, G. (1998). Secondary neutron and photon dose in proton therapy. *Radiotherapy and Oncology*, *48*(3), 293–305. https://doi.org/10.1016/S0167-8140(98)00049-8

Amin, T., Infantino, A., Barlow, R., & Hoehr, C. (2018). Validating production of PET radionuclides in solid and liquid targets: Comparing Geant4 predictions with FLUKA and measurements. *Applied Radiation and Isotopes*, *133*, 61–67. https://doi.org/10.1016/j.apradiso.2017.12.009

Anwer, M., Naz, A., Ahmad, I., Usman, M., Hussain, J., Ilyas, S. Z., & Shahid, M. (2022). Ion beam activation of natCu, natTi, natNi and measurement of product formation cross sections at low energy (<10 MeV). *Radiochimica Acta*, *110*(10), 799–808. https://doi.org/10.1515/ract-2021-1132

Arbabi, A., Sadeghi, M., & Joharifard, M. (2009). Irradiation and dosimetry of Nitinol stent for renal artery brachytherapy. *Applied Radiation and Isotopes*, *67*(1), 129–132. https://doi.org/10.1016/j.apradiso.2008.07.012

Battistoni, G., Boehlen, T., Cerutti, F., Chin, P. W., Esposito, L. S., Fassò, A., Ferrari, A., Lechner, A., Empl, A., Mairani, A., Mereghetti, A., Ortega, P. G., Ranft, J., Roesler, S., Sala, P. R., Vlachoudis, V., & Smirnov, G. (2015). Overview of the FLUKA code. *Annals of Nuclear Energy*, *82*, 10–18. https://doi.org/10.1016/j.anucene.2014.11.007

Blaha, J., La Torre, F. P., Silari, M., & Vollaire, J. (2014). Long-term residual radioactivity in an intermediate-energy proton linac. *Nuclear Instruments and Methods in Physics Research Section A Accelerators Spectrometers Detectors and Associated Equipment*, *753*, 61–71. https://doi.org/10.1016/j.nima.2014.03.058

Böhlen, T. T., Cerutti, F., Chin, M. P. W., Fassò, A., Ferrari, A., Ortega, P. G., Mairani, A., Sala, P. R., Smirnov, G., & Vlachoudis, V. (2014). The FLUKA Code: Developments and Challenges for High Energy and Medical Applications. *Nuclear Data Sheets*, *120*, 211–214. https://doi.org/10.1016/j.nds.2014.07.049

Chen, J. (2022). Nuclear Data Sheets for A=48. *Nuclear Data Sheets*, *179*, 1–382. https://doi.org/10.1016/j.nds.2021.12.001

Duerig, T., Pelton, A., & Stöckel, D. (1999). An overview of nitinol medical applications. *Materials Science and Engineering: A*, *273-275*, 149–160. https://doi.org/10.1016/S0921-5093(99)00294-4

Dughaish, Z. H. (1997). Effect of variation of proton beam energy on the martensitic transformation temperature of shape memory nitinol alloy. *Materials Letters*, *32*(1), 29–32. https://doi.org/10.1016/S0167-577X(97)00007-4

Eigler, N., Whiting, J., Li, A., Frimerman, A., Makkar, R., Hausleiter, J., Fishbein, M. C., Schwartz, R. S., & Litvack, F. (1999). Effects of a positron-emitting VANADIUM-48 nitinol stent on experimental

restenosis in porcine coronary arteries: An injury–response study. *Cardiovascular Radiation Medicine*, *1*(3), 239–251. https://doi.org/10.1016/S1522-1865(99)00029-3

Ferrari, A., Sala, P., Fasso, A., & Ranft, J. (2005). FLUKA: A Multi-Particle Transport Code. CERN Yellow report, 2005-10. Office of Scientific and Technical Information (OSTI). https://doi.org/10.2172/877507

Li, A. N., Eigler, N. L., Litvack, F., & Whiting, J. S. (1998). Characterization of a positron emitting V48 nitinol stent for intracoronary brachytherapy. *Medical Physics*, *25*(1), 20–28. https://doi.org/10.1118/1.598164

More, C. V., Akman, F., Dilsiz, K., Ogul, H., & Pawar, P. P. (2023). Estimation of neutron and gamma-ray attenuation characteristics of some ferrites: Geant4, FLUKA and WinXCom studies. *Applied Radiation and Isotopes*, *197*, 110803. https://doi.org/10.1016/j.apradiso.2023.110803

Morgan, N. B. (2004). Medical shape memory alloy applications—the market and its products. *Materials Science and Engineering: A*, *378*(1), 16–23. https://doi.org/10.1016/j.msea.2003.10.326

Muhammad, N., Adil, M., Mulk, S. U., Ahmad, I., Hussain, J., Abbas, T. A., Anwer, M., Makinaga, A., & Shahid, M. (2025). Proton and alpha-particle activation studies of natFe, natCu, natTi and natW targets at low energies. *Radiochimica Acta*, *113*(1), 9–21. https://doi.org/10.1515/ract-2024-0310

Nath, R., Amols, H., Coffey, C., Duggan, D., Jani, S., Li, Z., Schell, M., Soares, C., Whiting, J., Cole, P. E., Crocker, I., & Schwartz, R. (1999). Intravascular brachytherapy physics: Report of the AAPM Radiation Therapy Committee Task Group No. 60. *Medical Physics*, *26*(2), 119–152. https://doi.org/10.1118/1.598496

Pelliccioni, M. (2000). Overview of Fluence-to-Effective Dose and Fluence-to-Ambient Dose Equivalent Conversion Coefficients for High Energy Radiation Calculated Using the FLUKA Code. *Radiation Protection Dosimetry*, *88*(4), 279–297. https://doi.org/10.1093/oxfordjournals.rpd.a033046

Rafiei, M. M., Bartoloni, A., Parsaei, S., & Strigari, L. (2025). Comparative analysis of proton depth dose distribution in the Snyder head phantom: FLUKA vs GEANT4 physics models. *Radiation Physics and Chemistry*, *229*, 112532. https://doi.org/10.1016/j.radphyschem.2025.112532

Sadeghi, M., Ansari, Z., & Kakavand, T. (2012). Targetry for 48V production and the nuclear model calculation on the charge particle induced reaction on Ti target. *Journal of Radioanalytical and Nuclear Chemistry*, *293*(1), 7–12. https://doi.org/10.1007/s10967-012-1754-6

Sadeghi, M., Kiavar, O., Hosseini, S. H., Fatehi, R., & Tenreiro, C. (2011). Cyclotron production and parameters calculation of 48V Nitinol stent for renal arteries in brachytherapy. *Journal of Radioanalytical and Nuclear Chemistry*, *289*(2), 565–571. https://doi.org/10.1007/s10967-011-1138-3

Saud, S. N., Hamzah, E., Abubakar, T., Refaei, A., & Hosseinian, R. (2014). The Influence of γ-irradiation on the Structure and Properties of the Cu- 11.5 wt. % Al- 4 wt. % Ni Shape Memory Alloys. *Advanced Materials Research*, *845*, 128–132. https://doi.org/10.4028/www.scientific.net/AMR.845.128

Schneider, U., Agosteo, S., Pedroni, E., & Besserer, J. (2002). Secondary neutron dose during proton therapy using spot scanning. *International Journal of Radiation Oncology, Biology, Physics*, *53*(1), 244–251. https://doi.org/10.1016/S0360-3016(01)02826-7

Siddiqui, A., Hallén, A., & Usman, M. (2023). Proton Irradiation-Induced Displacement Damage in 650 v Si and SiC Power Diodes. *Physica Status Solidi (A)*, *220*(21), 2300300. https://doi.org/10.1002/pssa.202300300

Stoller, R. E., Toloczko, M. B., Was, G. S., Certain, A. G., Dwaraknath, S., & Garner, F. A. (2013). On the use of SRIM for computing radiation damage exposure. *Nuclear Instruments and Methods in Physics Research Section B: Beam Interactions with Materials and Atoms*, *310*, 75–80. https://doi.org/10.1016/j.nimb.2013.05.008

Şerban, A.-G., de la Torre González, J. A., Anguiano, M., Lallena, A. M., & Salvat-Pujol, F. (2025). On the improved performances of FLUKA v4-4.0 in out-of-field proton dosimetry. *Radiation Physics and Chemistry*, *237*, 112947. https://doi.org/10.1016/j.radphyschem.2025.112947

Tatar, C., & Zengin, R. (2005). The effects of γ-irradiation on some physical properties of Cu–13.5 wt.%Al–4 wt.%Ni shape memory alloy. *Materials Letters*, *59*(26), 3304–3307. https://doi.org/10.1016/j.matlet.2005.04.062

Wang, H., Yi, X., Zhu, Y., Sun, S., Gao, Y., Cai, W., & Gao, Z. (2018). Effects of proton irradiation on the microstructure and shape recovery characteristics of a NiTi alloy. *Materials Characterization*, *140*, 122–128. https://doi.org/10.1016/j.matchar.2018.04.001

Wang, Z. G., Zu, X. T., Liu, L. J., Zhu, S., Huo, Y., Lin, L. B., Feng, X. D., & Wang, L. M. (2003). Effect of 18 MeV proton irradiation on the R-phase transformation in TiNi shape memory alloys. *Nuclear Instruments and Methods in Physics Research Section B: Beam Interactions with Materials and Atoms*, *211*(2), 239–243. https://doi.org/10.1016/S0168-583X(03)01279-5

Yi, X., Sun, S., Sun, B., Zhao, Y., Ning, R., Zhang, S., Gao, Z., Wang, H., & Cai, W. (2022). Microstructure evolution and strain recovery characteristic of proton-irradiated Ti-rich NiTi thin films. *Progress in Natural Science: Materials International*, *32*(1), 72–78. https://doi.org/10.1016/j.pnsc.2021.10.004

Yu, Y., & Chen, Z. (2024). Study on induced radioactivity in proton therapy accelerators. *Radiation Physics and Chemistry*, *221*, 111751. https://doi.org/10.1016/j.radphyschem.2024.111751